

Electrochemical Properties of Commercially Pure Ti with TiB/TiB₂ Coatings in Hanks' Balanced Salt Solution

Adib Ebrahimi, Hamid Esfahani, Arash Fattah-alhosseini, and Omid Imantalab

(Submitted September 3, 2018; in revised form January 13, 2019; published online February 27, 2019)

In this study, in order to evaluate the electrochemical performance of different titanium boride coatings created on the commercially pure titanium (CP-Ti), distinct electrochemical assays in Hanks' balanced salt solution at 37 °C were conducted using pack cementation method. The results showed that the boriding at 900 and 1000 °C for 3 h creates the TiB whiskers and TiB whiskers/TiB₂ dense layer on the top of the commercially pure titanium surface, respectively. It was also found that not only borides coating had good adhesion on the substrate, but also that improved the titanium hardness more than five times. Polarization plots clarified the passive behavior of borided specimens. Impedance spectroscopy tests indicated the acceptable corrosion behavior of the borided specimens in Hanks' balanced salt solution. Mott–Schottky measurements indicated that the passive layers formed on the commercially pure titanium and the borided specimens had doped *n*-type semiconductor properties. Mott–Schottky measurements displayed that the donor density of the passive layers decreased with the rising time as well. Finally, because of better surface conditions to make a less defective and more protective passive layer, the borided specimen at 900 °C in comparison with the borided specimen at 1000 °C was shown to be the more suitable choice for bioimplant applications.

Keywords adhesion, Hanks' balanced salt solution, Mott–Schottky, passive layer, titanium boride

1. Introduction

High strength, low specific density and excellent biocompatibility of titanium make it one of the important metallic biomaterials (Ref 1, 2). Titanium itself develops a passive film and results in good corrosion resistance during implantation. However, if the passive film is broken under stresses of surrounding environment, the poor tribological properties are achieved. Hence, the poor tribological properties of titanium limit its biomedical feature in which titanium is used as a structural component. There are some attempts for developing titanium usages as articulating joints via surface modification of titanium (Ref 3). Among the surface modification methods, applying the biocompatible coatings is favorable to develop the metallic implants such as titanium and its alloys. Morphology, composition and also surface microstructure are considerably changed via coating procedure (Ref 4). Boriding or bronizing is an effective method to modify the titanium surface with regard to the formation of hard and excellent wear-resistant TiB, Ti₃B₄ and TiB₂ intermetallic phases. The several boriding methods such as laser ablation (Ref 5), plasma (Ref 6), molten-salt (Ref 7), electrochemical (Ref 8), fluidized bed reactor (Ref 9), and powder pack cementation (Ref 10) have been developed to increase the tribological and corrosion behaviors of Ti and its

alloys due to that the titanium borides (TiB₂, TiB, Ti₃B₄) have high melting point, high hardness values, high chemical and thermal stability (Ref 11). Boriding via pack cementation is a diffusion-based coating method which is increasingly applied due to the cost–benefit, simple process and specimen uses with any shape and geometry. In this method, the boride layers are formed in situ on top of the surface embedded in a boron source by heating the titanium substrate. Li et al. (Ref 12) found that the boriding at 905–1100 °C forms the dual layers on the titanium substrate, in which TiB₂ and TiB make the outer and inner layers, respectively. Keddam et al. (Ref 13) also observed the similar findings and reported that formation rates of TiB₂ and TiB layers obeyed the parabolic character. It is worth to mention that the alloy elements in the titanium alloys affect the thickness of TiB layer (Ref 14). The excellent coincidence of titanium borides thermal expansion coefficient with titanium substrate (the thermal expansion coefficients of Ti, TiB and TiB₂ are 8.6×10^{-6} , 8.5×10^{-6} and $8.1 \times 10^{-6} \text{ } ^\circ\text{C}^{-1}$, respectively) reduces any threats of distortion issued by thermal stress of heating and cooling (Ref 15, 16).

Recently, the boriding process has been applied on titanium and its alloys for biomedical applications. The titanium borides improve the growth of bone-like appetite on TiB₂/HA composite layer successfully, while they protect the titanium substrate against the abrasion (Ref 17). Ding et al. (Ref 18) evaluated the wear resistance of multilayer TiB/TiB₂ in Hanks' balanced salt solution, and they found out this material is a good suggestion for improving the wear resistance of artificial joints. Das et al. (Ref 19) investigated the effect of TiB on in vitro wear resistance of TiB–TiN coatings on Ti–6Al–4V alloy. They presented these composite coatings for using in load-bearing articulating surfaces due to the high stiffness and biocompatibility and excellent in vitro wear resistance.

In order to culture the animal cells, Hanks' balanced salt solution seems to be an artificial salt mixture that is mainly used in combining with naturally occurring body substances (tissue

Adib Ebrahimi, Hamid Esfahani, Arash Fattah-alhosseini, and Omid Imantalab, Department of Materials Engineering, Bu-Ali Sina University, Hamedan 65178-38695, Iran. Contact e-mail: a.fattah@basu.ac.ir.

extracts and blood serum) and/or more complex chemically defined nutritive solutions. As mentioned above, boriding modifies the surface properties of titanium implant leading to unknown electrochemical behavior toward the contact with ionic species of body fluids. To the best of our knowledge, there are a few reports on electrochemical properties of titanium borides in simulated body fluid (SBF) solutions (Ref 16). Titanium borides have shown complicated corrosion behavior in specific SBF, and a clear mechanism has not been reported yet. Therefore, the aim of this work is to explore the diversity of titanium borides (TiB and TiB/TiB₂) coatings effect on corrosion resistance of commercially pure titanium (CP-Ti) in Hanks' balanced salt solution. For this purpose, the CP-Ti was borided via pack cementation process followed by characterization to identify the morphology, microstructure, hardness and adhesion of titanium borides. After understanding the boriding conditions for obtaining the TiB and TiB/TiB₂ layers on the titanium surface, the electrochemical assays such open-circuit potential (OCP) measurement, Mott–Schottky (M–S), electrochemical impedance spectroscopy (EIS) and potentiodynamic polarization (PDP) tests were carried out in Hanks' balanced salt solution.

2. Experimental

2.1 Boriding Procedure

Prior to the boriding, the CP-Ti grade 2 (Fe: 0.12%, C: 0.009%, N: 0.013%, H: 0.0018%, O: 0.1% wt. and Ti-balance) coupons (0.2 × 1 × 2 cm²) were polished with 2000 sandpaper. To remove the contaminations and the air-formed oxide film, specimens were washed by solution containing 1 mL HF, 10 mL HNO₃ and 89 mL H₂O. The dried specimens were embedded in the boron powder source prepared by blending 50 wt.% B powder, 35 wt.% activated charcoal and 15 wt.% NaCO₃. The sealed packs were heated by a ramp of 8 °C/min and then soaked separately at 900 and 1000 °C for 3 h in the air atmosphere. After cooling in the furnace, corresponding specimens were called as TB900 and TB1000. For further investigations, the specimens were polished and etched in 96% H₂O + 2.5% HNO₃ + 1.5% HF solution.

2.2 Characterization of Boride Layers

A Philips X'Pert apparatus equipped with a copper anode (Cu-Kα λ = 1.5406 Å) was applied to provide the x-ray diffraction (XRD) patterns of borided samples. The micrographs of boride layers were taken by scanning electron microscopy (SEM model: FEI ESEM Quanta 200). ImageJ software (model: 1.38X, NIH-USA) was assigned to calculate the thickness of boride layers. For this matter, five different points of each sample were selected and SEM images were taken. The average of measurements was reported as the thickness of coating. The microhardness of CP-Ti and borided samples was measured by the Vickers indentation test at 100 kgf applied force for 20 s dwelling time by means of device model Buehler-Illinois-60044. Adhesion of boride layers was studied based on the Daimler–Benz method (Ref 20). For this matter, a Rockwell-C indenter with 3 mm diameter was used. The applied force of Rockwell-C indentation was 980 N for 30 s dwelling time. To ensure the reliable hardness and adhesion, five tests were carried out and the average

reported. The electrochemical behavior of pure and the borided CP-Ti samples (as the working electrodes) was assayed in a glass three-electrode cell composed of the reference electrode (an Ag/AgCl electrode), the auxiliary electrode (a platinum plate) and the working electrode in 250 ml of quiescent Hanks' balanced salt solution connected to a galvanostat/potentiostat set (μAutolab Type III/FRA2). The curve fitting of all EIS plots was performed by Nova software. Also, to ensure the reliable electrochemical behavior, five tests were carried out and the average reported.

2.3 Electrochemical Tests

Electrochemical measurements were studied in Hanks' balanced salt solution at a pH of 7.4 as a simulated body fluid at 37 °C. The Hanks' balanced salt solution was prepared by dissolving adequate amount of chemical reagents as given in Table 1 in distilled water at 37 °C (Ref 21). Before each electrochemical measurement, the surface preparation was followed by ultrasonic cleaning for 5 min in acetone and finally the samples were rinsed in distilled water and dried in cold air. The exposed area of the working electrodes was about 0.64 cm². First, the OCP variations of the working electrodes with respect to immersion time were registered until a surface stability was reached. Then, the PDP curves were scanned at 1 mV/s from –250 mV_{Ag/AgCl} versus OCP to 3000 mV_{Ag/AgCl}. The EIS tests were carried out at the OCP condition with a step rate of 10 point/decade in the applied frequency range of 100 kHz to 10 mHz by employing an alternating amplitude of 5 mV. The M–S measurement was scanned in the cathodic direction with a constant linear step of 25 mV and a fixed frequency of 10 kHz from 0.6 to –0.8 V_{Ag/AgCl}. In this study, each electrochemical test was repeated five times to check the reproducibility of the obtained electrochemical tests.

3. Results and Discussion

3.1 SEM Results

The cross-sectional view of borided samples at different heat treatments (900 and 1000 °C) is shown in Fig. 1(a) and (b). As can be seen in both micrographs, the top layer has been changed by boriding process and subsequently different morphologies were formed on top of the surface with regard to the different heat treatment conditions. The boride whiskers penetrated into titanium substrate are the main morphology along the top of the surface of borided specimen at 900 °C. At top of the surface borided at 1000 °C, not only the above whiskers are observed, but also a dense layer covering the

Table 1 Amount and composition of chemical reagents in Hanks' balanced salt solution (Ref 21)

Chemical reagent	Amount, g/L
NaCl	4.970
KCl	0.224
CaCl ₂	0.167
NaHCO ₃	0.250
NaH ₂ PO ₄ ·2H ₂ O	0.500
Glucose	0.072

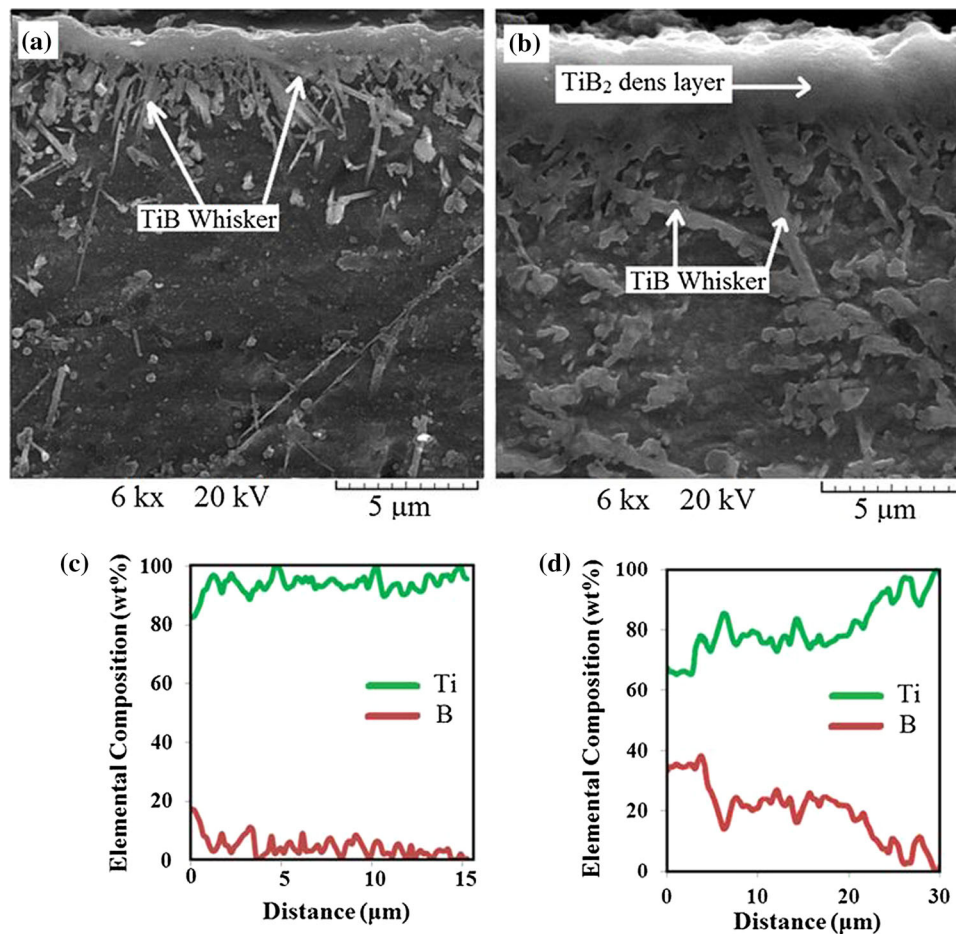


Fig. 1 SEM micrographs of titanium boride coating on CP-Ti: (a) TB900 and (b) TB1000. X-ray line analysis along the titanium boride layer: (c) TB900 and (d) TB1000

surface is found. In lower amount of the boron source, the TiB phase was the dominant phase, while by more diffusion of B atoms into the Ti substrate, the TiB₂ can be also formed. Hence, with increase in the boriding temperature from 900 to 1000 °C, coefficient of diffusion of B was intensified and therefore more B atoms could be penetrated into the substrate. The preferable oriented whiskers obtained in both samples belong to the TiB phase, and the dense layer which is found just in Fig. 1(b) is attributed to the TiB₂ phase (Ref 22, 23). The similar microstructure has been found in plasma paste brooding method (Ref 24). In addition, the thickness of covered boride layer was different. The average thickness of $1.0 \pm 0.1 \mu\text{m}$ and $2.3 \pm 0.2 \mu\text{m}$ was obtained in respect to the covered titanium borides at top of the surface of titanium borided at 900 and 1000 °C. Moreover, the TiB whiskers could grow via boriding at 1000 °C, in which the width of whiskers became three times more than those formed at 900 °C. Although it has been reported that the Ti₃B₄ phase may present in the binary TiB system (Ref 16), we could not mark it in the SEM micrographs. Figure 1(c) and (d) shows the elemental distribution of Ti and B along the substrate to surface borided at 900 and 1000 °C, respectively. A countercurrent distribution of B and Ti concentration is observed from the top surface to the depth. With respect to the atomic weight of Ti (47.8 g/mol) and B (10.8 g/mol), and also in accordance with the illustrations Fig. 1(c), it can be elucidated that the TiB was the dominant

titanium boride in surface of TB900. Furthermore, Fig. 1(d) shows the elemental composition of Ti and B remained constant across two steps. One step is given as the TiB₂ top layer, and other belongs to the under TiB whiskers. According to the micrographs, it was found that the boriding temperature had a significant effect on rendering diversity of titanium boride.

3.2 Phase Analysis of Boride Layers

The XRD patterns of titanium borided at 900 and 1000 °C are presented in Fig. 2(a). According to the standard card JCPDS, 01-075-0967 and also 01-073-2148, the XRD patterns revealed the presence of TiB and TiB₂ in both samples in addition to the Ti as the substrate. Since the thin layers of borides were formed on the titanium substrate, the Ti peaks were also detected in the XRD pattern of both samples. However, there is a difference in the diversity of TiB and TiB₂ in the mentioned samples. In order to understand the role of heat treatment of boriding on Ti substrate phase forming, XRD patterns were investigated in the higher magnifications. Figure 2(b) and (c) shows the higher magnification of XRD patterns of TB900 and TB1000 in the ranges of 33°-40° and 41°-45°, respectively. These ranges are interested in studying because the characteristic main peaks of TiB and TiB₂ are observed at $2\theta = 35.295^\circ$ and $2\theta = 44.477^\circ$, respectively. The observation of (011) planes and double (210) and (102) planes

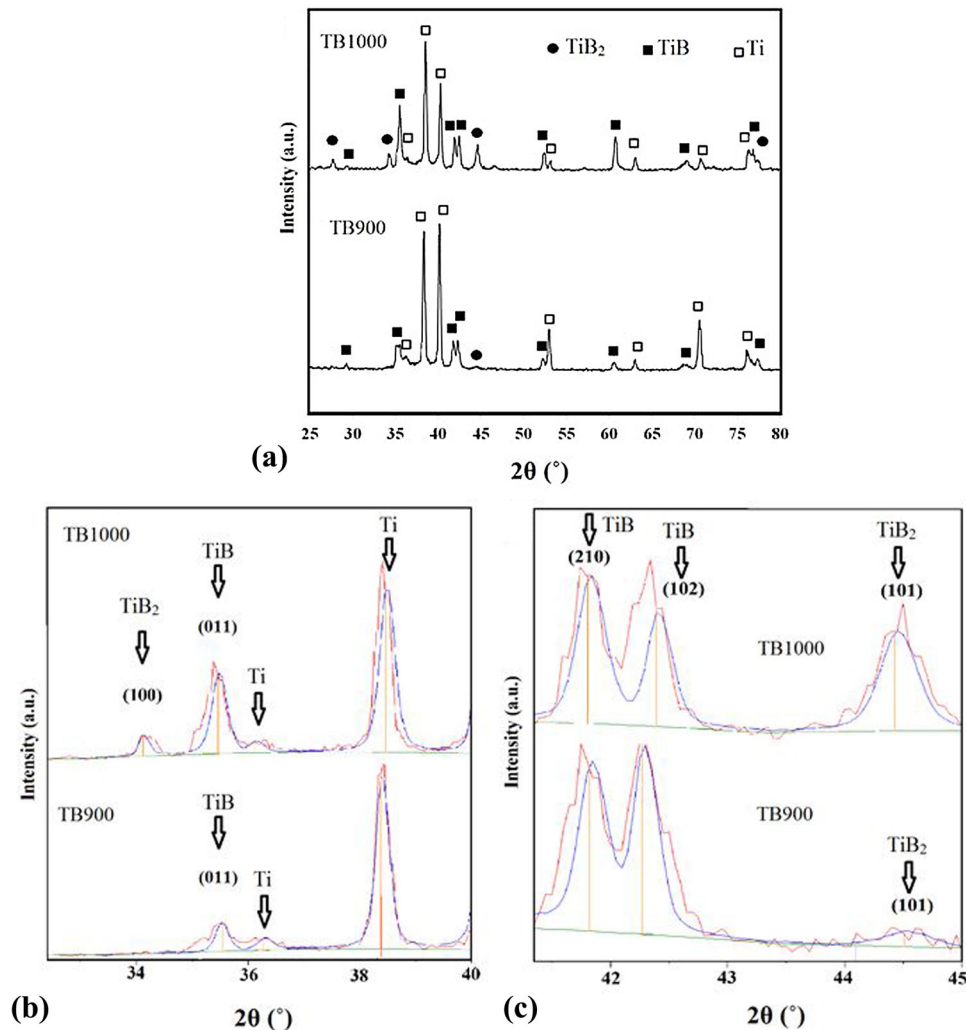


Fig. 2 (a) XRD patterns of TB900 and TB1000. Higher magnification of XRD patterns in the range of (b) 33°-40° and (c) 41°-45°, and deconvoluted patterns regarding the TiB and TiB₂ peaks

in the pattern of both samples confirmed the formation of TiB. Although the peak corresponding to diffraction of (101) planes in TiB₂ lattice was identified in both patterns, it should be explained that it has low intensity in TB900 pattern. Hence, the ratio of intensity of (101)_{TiB₂} per intensity of (102)_{TiB} may be useful. It was found that the crystallinity of TiB₂ in TB1000 was about six times more than one in the TB900. Furthermore, the XRD pattern of TB900 in the range of 33°-40° does not display a diffraction with regard to the (100)_{TiB₂}. Therefore, it can be assumed that the TiB is issued by heat treatment at 900 °C, and TiB/TiB₂ is obtained over treatment at 1000 °C. The SEM micrographs and also elemental composition analysis almost confirmed the above finding. It is worth mentioning that a peak corresponding to the Ti₃B₄ was not detected in XRD patterns too.

3.3 Hardness and Adhesion of Boride Layers

Prior to evaluating the corrosion resistance of TiB and TiB/TiB₂ composite layers against the harsh body fluid such as Hanks' balanced salt solution, attention to the mechanical properties of coating such as hardness and adhesion to the substrate may be helpful. The roughness analysis (longitudinal

Table 2 Roughness analysis of bare and boronized titanium (longitudinal)

Roughness parameters	TB900	TB1000	Bare Ti
R_a , μm	0.732	0.842	0.257
R_z , μm	3.993	6.218	2.205
R_{32} , μm	2.349	3.095	0.952
R_{zlis} , μm	2.54	3.41	1.19
R_{sm} , mm	0.06	0.07	0.06

and transversal) of bare Ti, TB900 and TB1000 was performed, and the obtained results are given in Tables 2 and 3. The hardness of TB900 and TB1000 was measured, and the obtained results are given in Table 4. As can be seen, it was found that the hardness of titanium surface was enhanced from 340 ± 10 HV to 1064 ± 30 and 1680 ± 20 via boriding at 900 and 1000 °C, respectively. The different value obtained for the surface hardness comes from the diversity of boride layers; the TiB whiskers were armed by the dense TiB₂ top layer in the

TB1000. The similar hardness values for TiB and TiB₂ were reported by the others (Ref 25, 26).

The adhesion of boride layers to the titanium substrate was evaluated by the Daimler–Benz method. According to this method, adhesion can be classified as HF1 to HF6 references regarding the developed cracks and delaminated areas around the indent as shown in Fig. 3(a).

With progress of more cracks and observation of exposed surface, the low adhesive coating is recognized (HF1 converts to HF6). The optical micrographs of TB900 and TB1000 after indentation are depicted in Fig. 3(b) and (c). Findings showed that no microcracks were produced by indentation, and also delamination was not occurred. In comparison with the HF standards, the results reveal that the TiB and also TiB/TiB₂ composite layers obey an overqualified HF1 standard corresponding to the overadequate adhesion. The similar findings have been observed for other ceramic coatings on the titanium substrate (Ref 27, 28). The penetrated TiB whiskers into the titanium substrate pinned the boride layer and subsequently improved the adhesion by the mechanical binding. In addition, the hard TiB₂ top layer (in sample TB1000) could resist against the fracture and so it also represented the high adhesion for TiB/TiB₂ composite layer. According to the boride layers characterizations summarized in Table 4, it can be said that a thin hard boride layer with high adhesion to titanium substrate was formed, and the arrangement and diversity of the boride composition would be main factors influencing the electrochemical properties of borided titanium via immersing in the body fluids.

3.4 Electrochemical Tests

3.4.1 Curves of Potentiodynamic Polarization and OCP. Figure 4 represents the evaluation of OCP changes with the exposure time in quiescent Hanks' balanced salt solution for CP-Ti and the borided samples during the first hour. It is observed that OCP values varied directly with exposure time in all cases representing the instinctive formation of the protective passive film on the surface of the specimens in

the studied system (Ref 29). Furthermore, it can be seen that the OCP values of the specimens varied slightly with increasing exposure time after 3400 s which demonstrates the proper surface condition (surface stability) prepared to implement the

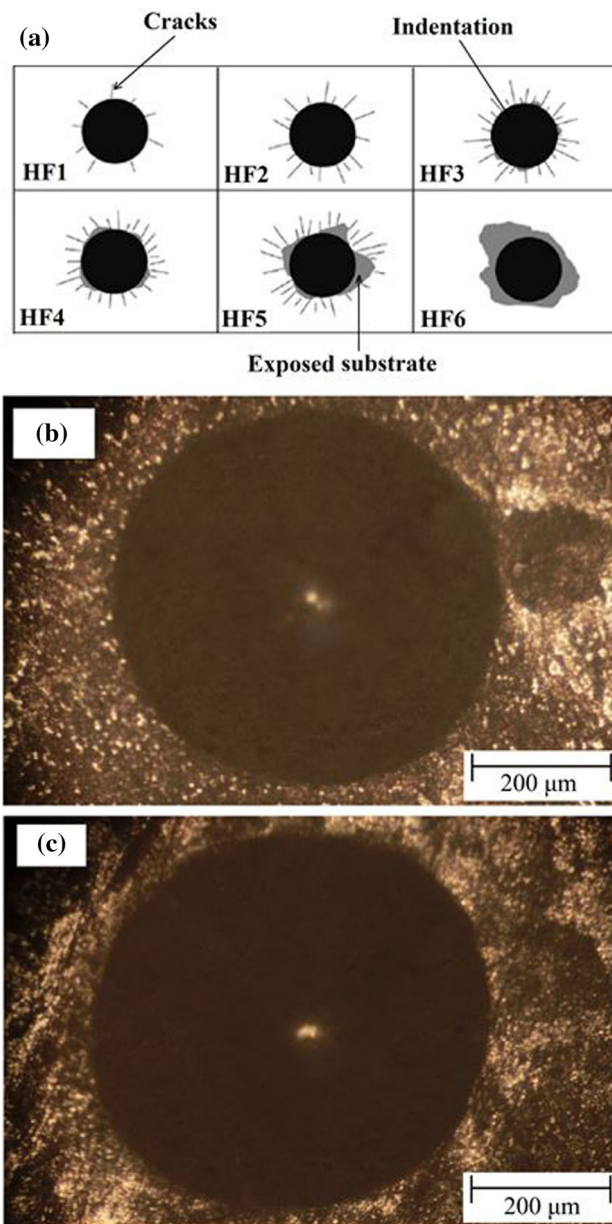


Fig. 3 Daimler–Benz adhesion chart (a) and optical microscopy images of Rockwell-C indentation on borided samples (b) TB900, and (c) TB1000

Table 3 Roughness analysis of bare and boronized titanium (transversal)

Roughness parameters	TB900	TB1000	Bare Ti
R_a , μm	0.503	1.172	0.233
R_z , μm	3.589	8.173	2.287
R_{32} , μm	2.723	3.921	1.2
R_{zJis} , μm	2.84	4.59	1.39
R_{sm} , mm	0.03	0.06	0.03

Table 4 Specifications of boride layer formed on the titanium surface via pack cementation method

Sample code	Boride layer specifications			
	Composition	Thickness, μm	Microhardness (HV)	Adhesion Ref.
TB900	TiB	1 ± 0.1	1064 ± 30	HF1
TB1000	TiB/TiB ₂	2.3 ± 0.2	1680 ± 20	HF1

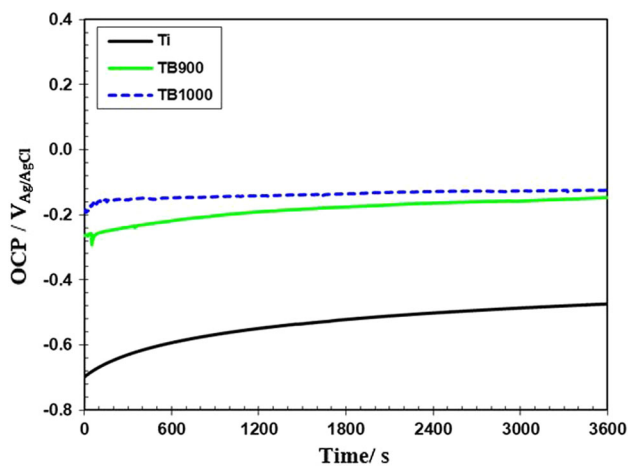


Fig. 4 OCP plots of Ti, TB900 and TB1000 specimens in Hanks' balanced salt solution

electrochemical measurements (Ref 30). The investigation conducted by Shukla et al. (Ref 31) has revealed the OCP values of CP-Ti and Ti-6Al-4V alloy stabilized after 3600 s of immersion time in Hanks' balanced salt solution. Moreover, Fattah-alhosseini et al. (Ref 30) and Sivakumar et al. (Ref 16) have reported that the OCP values of CP-Ti and the borided CP-Ti reach a stable status after 1 h in Ringer's solution. As seen in Fig. 4, the stable OCP values of the borided CP-Ti specimens are more positive than those of CP-Ti specimen which is consistent with the reported results in the references (Ref 16, 32). In addition, according to Fig. 4, it is worth mentioning that there were no traces of surface metastability (the oscillations in the OCP values) in the spontaneous passive films developed on the surface of the borided CP-Ti specimens. Hence, it can be noted that the coatings free of pores/cracks were carried out on CP-Ti specimens by the boriding process in the present work (Ref 16).

Figure 5 indicates the potentiodynamic polarization plots recorded after 1 h of exposure to quiescent Hanks' balanced salt solution under OCP condition for CP-Ti and the borided specimens. The electrochemical parameters derived from Fig. 5, namely the corrosion current density (i_{corr}) and corrosion potential (E_{corr}), are presented in Table 5. In this study, the current density values were achieved by extrapolating the linear Tafel segments of the cathodic polarization plots. According to Fig. 5, it is apparent that the surface of the studied samples is able to form a passive layer in Hanks' balanced salt solution. Also, CP-Ti resisted the breakdown of the passive film at potentials above $2.0 V_{\text{Ag/AgCl}}$, while the borided samples indicated the passive film breakdown and transpassive characterization at a potential of lower than $2.0 V_{\text{Ag/AgCl}}$. These results are consistent with the potentiodynamic polarization behavior of CP-Ti and the borided specimens in SBF solutions reported in published papers (Ref 16, 32, 33). It is reported that the passive breakdown of the borided specimens in a simulated body fluid solution is caused by localized corrosion sites at high potentials during the potentiodynamic polarization measurements (Ref 16). It is noteworthy that the in vivo potential range of CP-Ti and its alloys is in the range of $+0.495 V_{\text{Ag/AgCl}}$ to $+0.590 V_{\text{Ag/AgCl}}$ (Ref 16, 33, 34). Hence, the borided specimens in this study are capable of being used as a bioimplant material because the breakdown potential of the specimens (as can be seen in Fig. 5) is higher than

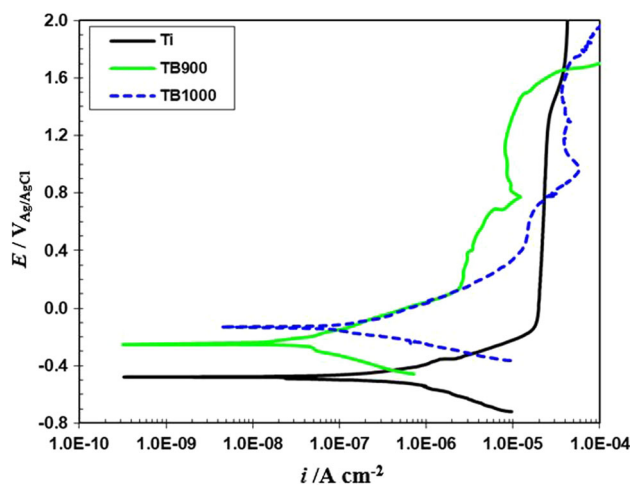


Fig. 5 PDP curves of Ti, TB900 and TB1000 specimens after 1 h of stabilization in Hanks' balanced salt solution

Table 5 Electrochemical data obtained from the PDP plots of CP-Ti and borided samples at 900 and 1000 °C in Hanks' balanced salt solution

	Bare Ti	TB900	TB1000
E_{corr} , mV	-477 ± 9	-253 ± 5	-131 ± 7
i_{corr} , $\mu\text{A}/\text{cm}^2$	0.35 ± 0.09	0.03 ± 0.01	0.21 ± 0.05
β_a , mV/dec	108 ± 0.04	145 ± 0.11	125 ± 0.04
β_c , mV/dec	-127 ± 0.09	-174 ± 0.15	-104 ± 0.07

+ $0.590 V_{\text{Ag/AgCl}}$. Moreover, it can be noted that the boriding process in this study had a positive effect on the performance of CP-Ti as an implant in Hanks' balanced salt solution (Ref 16, 33, 34). Comparing the reported data in Table 5, the TB1000 specimen corroded at a much higher current density ($0.20 \mu\text{A}/\text{cm}^2$) than the TB900 specimen ($0.03 \mu\text{A}/\text{cm}^2$). Accordingly, the highest corrosion current density pertains to the CP-Ti ($0.35 \mu\text{A}/\text{cm}^2$).

3.4.2 EIS Measurements. To assess the passive behavior of CP-Ti and the borided specimens in Hanks' balanced salt solution as a function of exposure time, EIS technique as an efficient, rapid, powerful, convenient and surface state-sensitive method was performed (Ref 30, 35, 36). Figure 6 shows the EIS plots after exposing the studied specimens in Hanks' balanced salt solution for different OCP immersion times. Considering the Nyquist curves in Fig. 6(a), (c) and (e), in all cases, the diameter of the imperfect semicircles became larger with exposure time to the studied solution. It is worth mentioning that the increment of the diameters in the Nyquist curves is an evidence of the better electrochemical corrosion behavior (Ref 32). It is observed from the Bode-phase curves of Fig. 6(b), (d) and (f) that the maximal phase angles (less than -90°) deviated from the behavior of an ideal capacitance (pure capacitance). Again, the behavior of a non-ideal capacitance is characterized by incomplete semicircles in the Nyquist curves. In general, the constant phase element (CPE) is substituted in the electrical equivalent circuits (EECs) in lieu of the pure capacitance (C) and the Warburg impedance (W) to

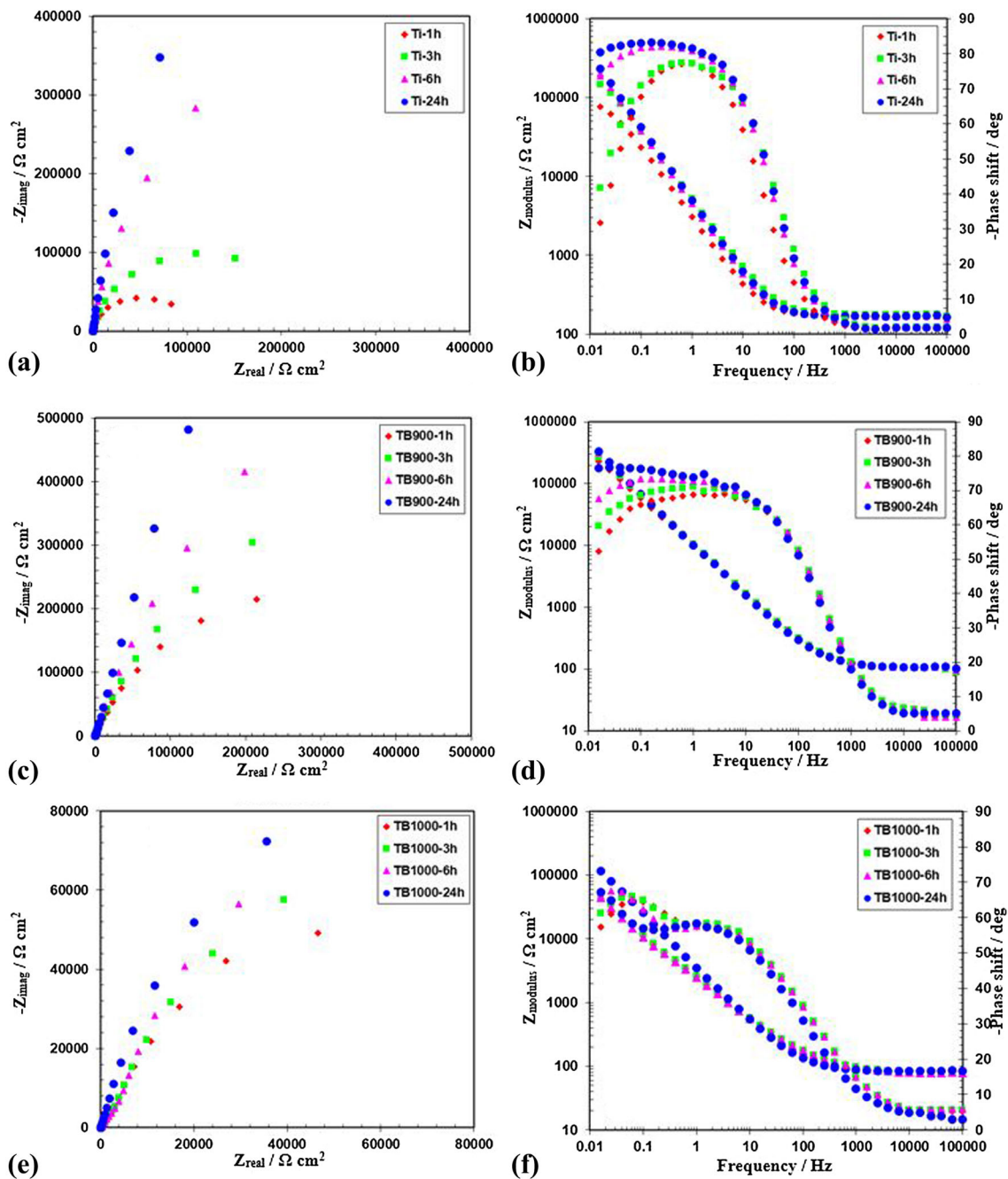


Fig. 6 Nyquist and Bode plots in respect to the (a, b) Ti, (c, d) TB900 and (e, f) TB1000 after different immersion times

get a perfect fit between theoretical and experimental data (Ref 37). Surface heterogeneities of the working electrode (such as roughness, adsorption of ions, the effect of resistivity variations of the covering film and scratches), the presence of pores in the oxide film and specific active sites (such as grain boundaries and impurities) are some of the well-known reasons for the appearance of a CPE behavior (Ref 30, 38-41). According to the Bode-phase curves of CP-Ti specimen in Fig. 6, the EIS spectra of this specimen need to be fitted by an EEC with one CPE. Additionally, the Bode-phase spectra of the borided specimens display the presence of two CPEs. The Bode-phase and Bode spectra of the studied specimens represent that the values of phase angles and absolute impedance are frequency

independent at high frequencies which express a pure resistance behavior (the resistance of the solution) (Ref 16, 29, 31, 42). Furthermore, a linear slope close to -1 from median- to low-frequency range as a sign of capacitance response of surface oxide film is seen in the Bode spectra of the studied samples (Ref 31). Considering the Nyquist curves of Fig. 6, it is plainly denoted that the corrosion resistance of the studied specimens was ameliorated by increasing exposure time from 1 to 24 h. Similar results were reported by other researches (Ref 29). Fattah-alhosseini et al. (Ref 29) studied the influence of exposure time on the electrochemical behavior of pure Ti and nano-grained pure Ti in Ringer's solution and found that the thickness of passive films was increased by increasing the

exposure time. Also, amelioration of the passive layers on CP-Ti after 24 h of exposure to Hanks' balanced salt solution was reported by Shukla et al. (Ref 31). Kramers–Kronig (KK) transformations of the real and imaginary axes of impedance are a straightforward criterion to acknowledge the EIS experimental data and assess the linear system theory (Ref 43). The niceties of this criterion were presented in the studies (Ref 44, 45). In these studies, the experimental EIS results of the studied samples after 1 h of exposure to Hanks' balanced salt solution were compared with the K-K transformations (Fig. 7). Considering good adaption between the experimental data and K-K transformations in Fig. 7, it is plainly denoted that during the EIS test the system conformed to the linear system theory. The experimental EIS data (Fig. 6) were simulated by using an adaptable EEC. The EEC model with two CPEs has been used to justify the EIS spectra of the borided pure Ti and Ti-6Al-4V alloy in SBF solutions by other researchers (Ref 16, 32, 33). According to the interpretation of the EIS behavior of the borided CP-Ti samples in published papers (Ref 16, 32), it can be noted that a double-layered passive film (comprising a porous film and a dense film) forms on the borided CP-Ti sample in SBF solutions. Figure 8 represents the applied EECs for curve fitting of the impedance spectra for (a) CP-Ti and (b) the borided specimens. The EECs in Fig. 8 were selected based on general shapes of the experimental EIS spectra, accessible

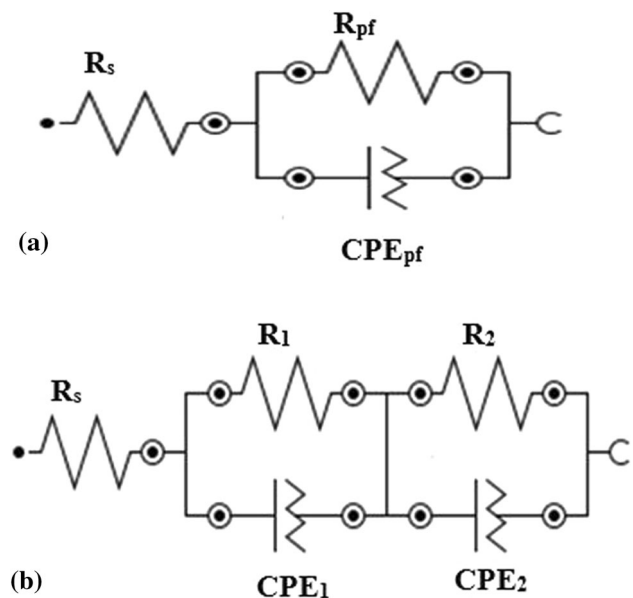


Fig. 8 EECs for the simulation of the impedance curves of (a) CP-Ti and (b) the borided samples

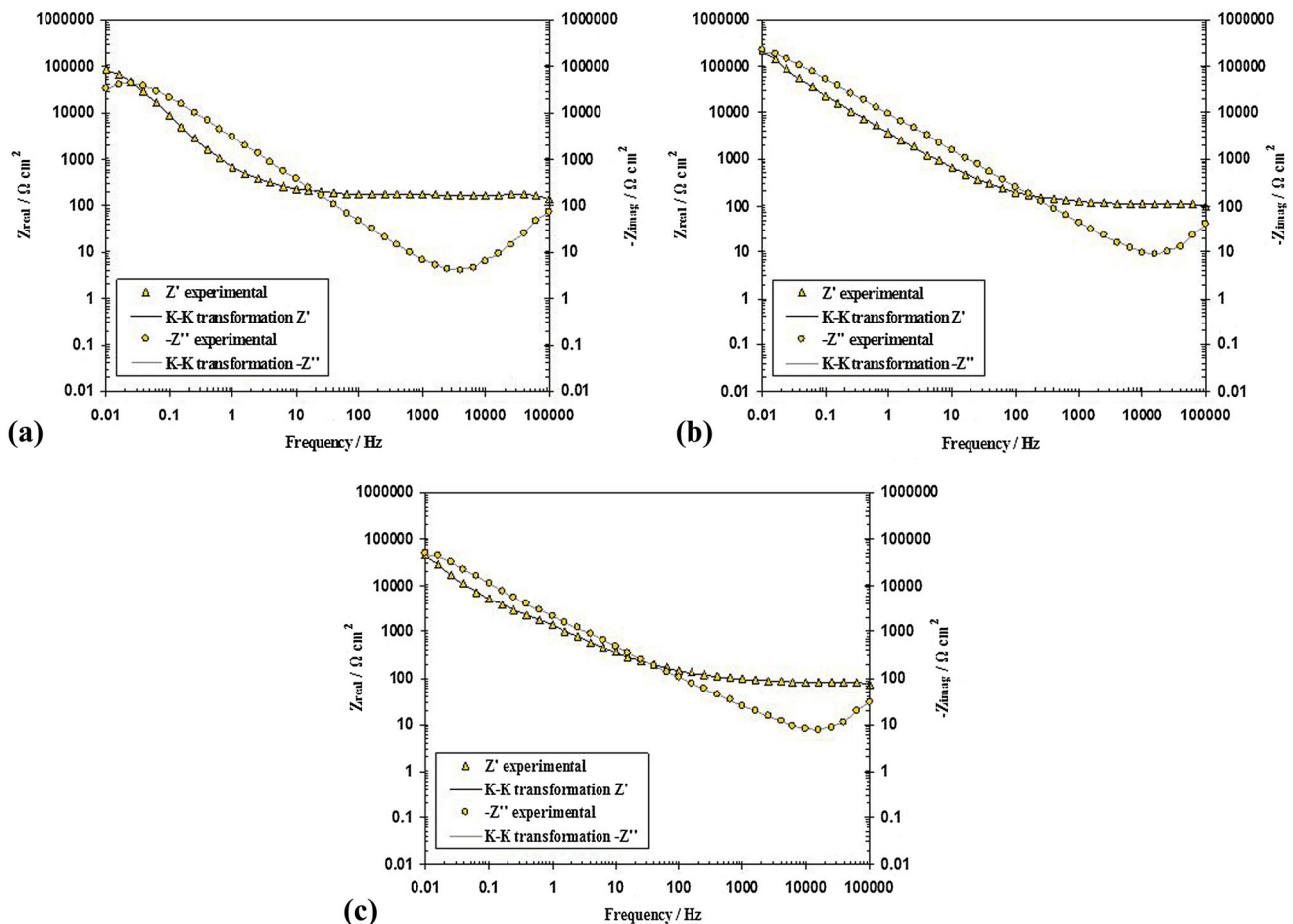


Fig. 7 KK transformations plots of the impedance curves obtained after 1 h of stabilization in Hanks' balanced salt solution. (a) CPTi, (b) TB900 and (c) TB1000

information on EECs selected previously for curve fitting of pure Ti and the borided CP-Ti in SBF solutions (Ref 16, 29, 31-33) and the Chi-square value (χ^2) to justify the EIS results. In these EECs, R_s marks the solution resistance, R_1 , R_2 , CPE_1 and CPE_2 are the outer/porous oxide film, the inner/dense oxide film, CPE of the outer film and CPE of the inner film, respectively, and R_{pf} and CPE_{pf} index the compact oxide film and CPE of the compact oxide film, respectively. The expression of a CPE is given as follows (Ref 46-48):

$$Z_{CPE} = \frac{1}{Q(j\omega)^n} \quad (\text{Eq 1})$$

where Q is a frequency independent parameter (in the frequency space for $0.5 < n < 1$, which indicates the distribution of the dielectric relaxation times), j indexes the imaginary unit, ω denotes the angular frequency and n indexes an adjustable parameter related to deviation from the behavior of pure capacitance.

The values of EEC elements corresponding to CP-Ti and the borided specimens are summarized in Table 6 versus exposure time to quiescent Hanks' balanced salt solution. Considering the obtained values (Table 6) according to EECs of Fig. 8, the inner oxide films of the borided samples represent remarkably higher resistance compared to the outer oxide films and also show the formation of compact and dense TiO_2 inner films and porous outer films on surfaces of the borided samples in the studied environment. It should be noted that the lower resistance of the outer oxide films represents the diffusion process occurring in these films. In addition, ascending trend is observed for both inner and outer oxide films resistant of the borided samples with an increase in immersion time. The similar trend which was reported for the passive resistance values (R_{pf}) corresponding to CP-Ti sample (Table 6) can be attributed to the compact oxide film growth on surface of this sample in the studied solution. Considering the polarization resistance values of the studied samples (R_p), it is plainly indicated that the TB900 sample (at each specified immersion time) displays the best electrochemical behavior as it has the highest polarization resistance values compared to the other studied samples. It must be mentioned that for bare CpTi (with one time constant), the polarization resistance (R_p) = R_{pf} , but for borided specimens (with two time constants) the polarization resistance (R_p) = $R_1 + R_2$. According to the aforementioned results in the present work, it can be concluded that the

TB900 specimen has the effective surface to form oxide film with the effective performance in Hanks' balanced salt solution. It should be mentioned again that the XRD results (Fig. 2) documented the formation of the TiB and TiB/TiB₂ layers on surface of CP-Ti by boriding process at 900 and 1000 °C for 3 h, respectively.

3.4.3 M-S Assays. Considering the point defect model (PDM), it is well known that the existent point defects in the oxide passive layer are classified into three kinds, involving the cation vacancies, the cation interstitials and the anion vacancies, which describe the passive layer breakdown, dissolution and growth mechanisms (Ref 49-51). According to PDM, the formation of the passive film on the metals was derived from generating and annihilating oxygen vacancies at the layer/metal and layer/solution interface, respectively. Hence, the density of the defects in the passive films is an interesting subject which was investigated by many researchers (Ref 49-54). This subject can be studied by the in situ M-S assay. In this assay, the barrier passive film capacitance (C) is estimated as a function of the applied electrode potential (E). Moreover, donor density (N_D for n -type semiconductor) can be calculated by the positive M-S slope and the following simple formula (Ref 51-54):

$$\frac{1}{C^2} = \frac{2}{\epsilon\epsilon_0 e N_D} \left(E - E_{FB} - \frac{k_B T}{e} \right) \quad (\text{Eq 2})$$

where ϵ indexes the passive film dielectric constant ($\epsilon = 60$ for Ti), e marks the charge of an electron (1.6×10^{-19}), ϵ_0 is symbol of the vacuum permittivity (8.854×10^{-12} F m⁻¹), T is mark of the absolute temperature (K) and E_{FB} is sign of the flat band potential (V) and k_B indexes the Boltzmann's constant (1.38×10^{-23} J K⁻¹).

Figure 9 displays the M-S plots of the studied specimens registered after the immersion time of 1 and 24 h in Hanks' balanced salt solution. As indicated in Fig. 9, the positive linear slope was recorded for all samples, which represents that the passive layers that developed on surfaces of the specimens in Hanks' balanced salt solution behave as n -type semiconductors. The semiconducting behavior of the passive film on pure Ti in SBFs (Hanks' balanced salt and Ringer's solution) was studied by Fattah-alhosseini et al. (Ref 29, 55), indicating that it acts like an n -type semiconductor. Considering the obtained data (Table 7) according to the linear regions and the positive slopes of M-S curves (N24/N1 implies donor density ratio), donor

Table 6 Values of EEC elements corresponding to CP-Ti and the borided specimens as a function of immersion time in Hanks' balanced salt solution

Sample Immersion time	Bare Ti				TB900				TB1000			
	1 h	3 h	6 h	24 h	1 h	3 h	6 h	24 h	1 h	3 h	6 h	24 h
$R_s, \Omega \text{ cm}^2$	167.86	169.32	164.47	166.54	110.13	108.70	110.12	109.68	80.53	78.63	77.96	77.28
$R_1 (\times 10^5 \Omega \text{ cm}^2)$					0.001	0.001	0.001	0.005	0.064	0.069	0.086	0.115
$Q_1 (\times 10^{-4} \text{ S}^2/\Omega \text{ cm}^2)$					1.440	1.050	0.810	0.730	1.710	1.490	1.780	1.480
n_1					0.78	0.77	0.78	0.79	0.61	0.61	0.62	0.67
$R_2 (\times 10^5 \Omega \text{ cm}^2)$					7.090	13.100	23.900	88.600	1.150	1.670	2.030	4.700
$Q_2 (\times 10^{-4} \text{ S}^2/\Omega \text{ cm}^2)$					0.230	0.215	0.210	0.212	1.640	1.640	1.730	1.270
n_2					0.94	0.97	0.89	0.89	0.94	0.92	0.95	0.96
$R_{pf} (\times 10^5 \Omega \text{ cm}^2)$	1.00	2.35	2.85	4.55								
$Q_{pf} (\times 10^{-4} \text{ S}^2/\Omega \text{ cm}^2)$	0.614	0.500	0.409	0.368								
n_{pf}	0.91	0.91	0.92	0.93								
$R_p (\times 10^5 \Omega \text{ cm}^2)$	1.00	2.35	2.85	4.55	7.091	13.101	23.901	88.605	1.214	1.739	2.116	4.815
Chi square	0.011	0.011	0.006	0.003	0.105	0.013	0.070	0.007	0.008	0.015	0.095	0.101

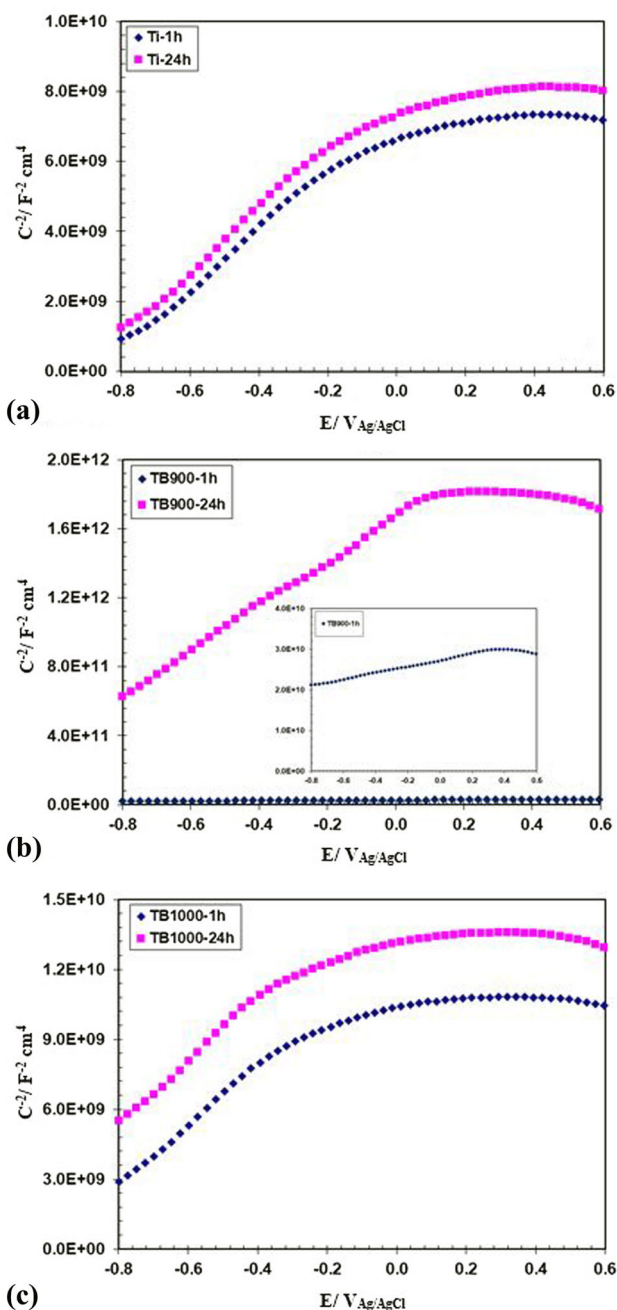


Fig. 9 M–S plots of (a) CP-Ti and (b, c) TB900 and TB1000 after 1 and 24 h in Hanks' solution

Table 7 Variations in donor concentration of CP-Ti and the borided samples in Hanks' balanced salt solution during the first 24 h

	Bare Ti	TB900	TB1000
$N_D(24 \text{ h})/N_D(1 \text{ h})$	0.940	0.006	0.950

concentration of the passive layers of all specimens by 1 h (N_1) to 24 h (N_1) in Hanks' balanced salt solution under OCP condition decreases, indicating that the electrochemical reactions decrease at the metal/solution interface, thereby increasing the compaction and stability of the passive layers with the

immersion time (Ref 56). Also, a remarkable decrease in the donor concentration of the passive film on TB900 specimen is noticeable after 24 h of immersion in Hanks' balanced salt solution.

3.5 Surface Observations

To understand the effect of immersion in Hanks' balanced salt solution on the microstructure of surface of borided samples, the SEM images were taken from the surface of TB900 and TB1000 before and after 7 days of immersion (see Fig. 10). The results show that the surface of TB900 has been not changed drastically, while some grooves are seen at the surface of TB1000. These microstructures confirm that how the monolithic TiB coating protects the pure titanium higher than TiB/TiB₂ coating in Hanks' balanced salt solution. As explained above, the lower resistance of TB1000 against the Hanks' balanced salt solution was because of the release of TiB₂ particles from the surface and also low stable passive layer.

The boron affects the impermeable TiO₂ passive film by creating defects; thus in the boronized samples, localized sites are available for the passivity breakdown. The corrosion reactions of TiB₂ may lead to the dissolution of the compound and formation of a boric acid (e.g., H₃BO₃) and titanium dioxide (TiO₂) where the latter is an insoluble compound (Ref 16, 33, 57, 58). The corrosion reactions occurring in this process can be (Ref 16, 33):

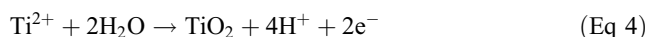


Figure 11 shows the EDS spectra from the surface of TB900 and TB1000 before and after the immersion in Hanks' balanced salt solution. The EDS spectra confirmed the formation of the oxide layer on the surface of both borided samples after the immersion (Fig. 11b and d). The reasonable oxygen peak which was identified in those spectra demonstrates the formation of the oxide layer on top of the samples. In addition to the B and Ti, Cl and Na elements were also detected regarding the precipitants from Hanks' balanced salt solution.

4. Conclusion

Two different boride layers TiB and TiB/TiB₂ were coated on the commercially pure titanium via pack cementation method under different heat treatment conditions. The results of XRD and SEM indicated that the boriding at 900 °C for 3 h caused to form TiB whiskers pretreated into the Ti substrate, and treatment at 900 °C for the similar soaking time created the TiB whiskers covered by dense TiB₂ layer. The hardness value of borided samples was obtained in 1064 ± 30 and 1680 ± 20 in respect to the boriding at 900 and 1000 °C. It was observed that both boride layers had good adhesion to the titanium substrate. The potentiodynamic polarization plots revealed that the all samples had passive behavior in Hanks' balanced salt solution. The electrochemical study on the borided samples also showed the better corrosion resistance compared to the pure titanium. Further investigations by electrochemical impedance spectroscopy showed that specimen borided at 900 °C had the highest polarization resistance. The results of Mott–Schottky indicated that the passive layer on the TiB and TiB/TiB₂

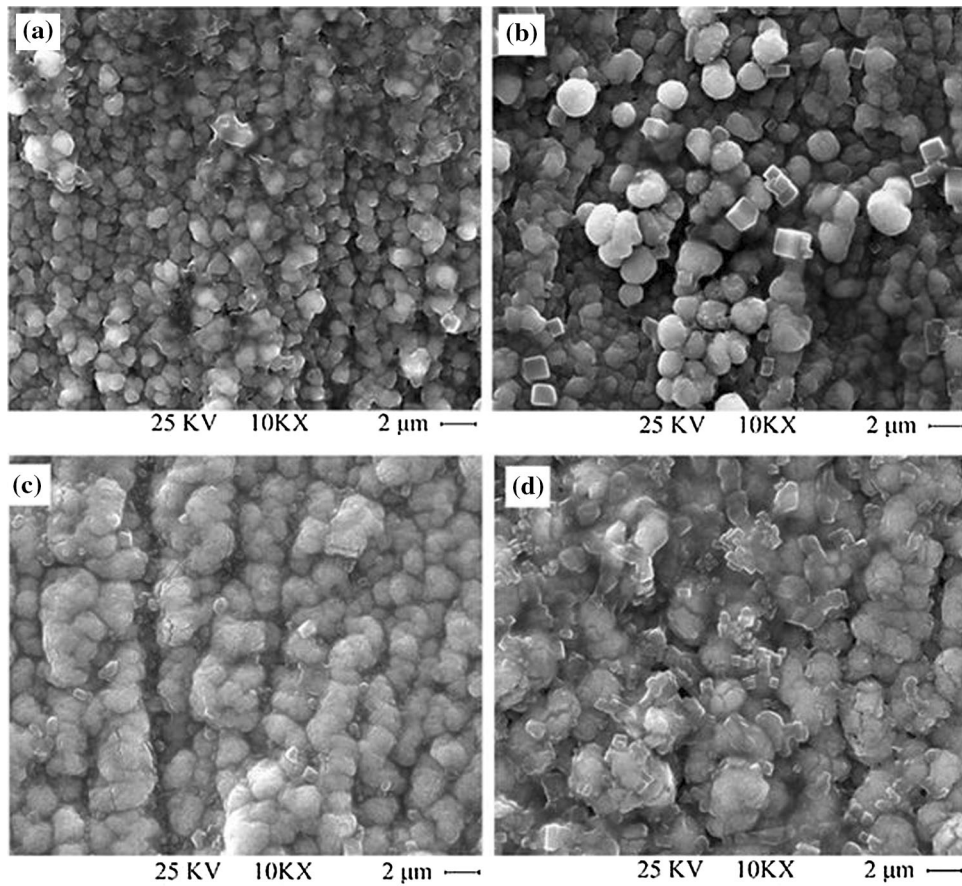


Fig. 10 SEM images of TB900 and TB1000 before (a, c) and after (b, d) 7 days of immersion in Hanks' balanced salt solution

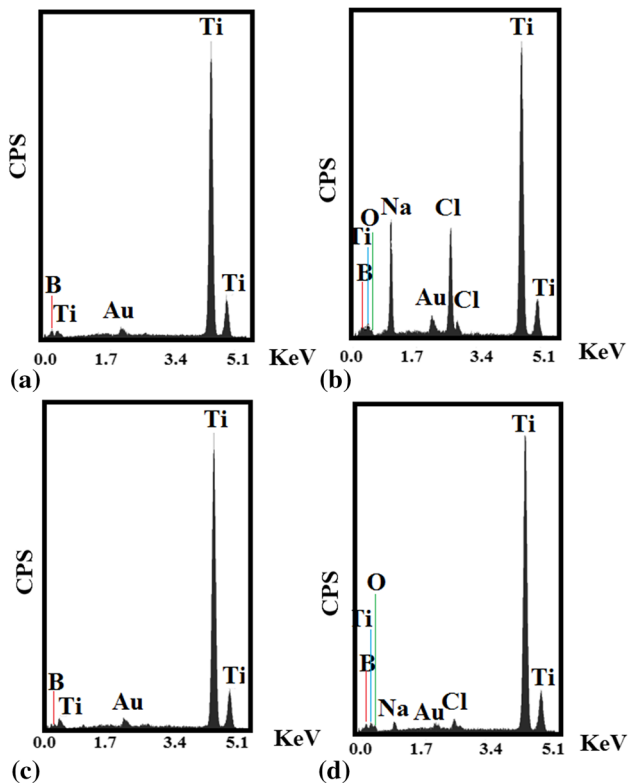


Fig. 11 EDS results of TB900 and TB1000 before (a, c) and after (b, d) 7 days of immersion in Hanks' balanced salt solution

coatings behaves such an *n*-type semiconductor. It was also found that the compaction of the passive layer was related to the reduction of donor density in the passive layer. According to the electrochemical studies, it can be concluded that the TiB coating resists higher than TiB/TiB₂ coatings in a harsh environment such as Hanks' balanced salt solution. Eventually, it can be suggested that the boriding of CP-Ti at 900 °C for 3 h makes a good adhesive coating in which it is suitable for biomedical applications.

Acknowledgments

This research was supported by the Iran National Science Foundation (INSF) with Project No. 95841122.

References

1. M.M. Stevens, *Biomaterials for Bone Tissue Engineering*, *Mater. Today*, 2008, **11**, p 18–25
2. C.M. Wu, P.W. Peng, H.H. Chou, K.L. Ou, E. Sugiarno, C.M. Liu, and C.F. Huang, *Microstructural, Mechanical and Biological Characterizations of the Promising Titanium tantalum Alloy for Biomedical Applications*, *J. Alloys Compd.*, 2018, **735**, p 2604–2610
3. S. Ramakrishna, M. Ramalingam, T.S. Sampath Kumar, and W.O. Soboyejo, *Biomaterials: A Nano Approach*, CRC Press, London, 2010, ISBN 9781420047813
4. V. Peretti, S. Ferraris, G. Gautier, C. Hellmich, O. Lahayne, B. Stella, S. Yamaguchi, and S. Spriano, *Surface Treatments for Boriding of*

- Ti6Al4V Alloy in View of Applications as a Biomaterial, *Tribol. Int.*, 2018, **128**, p 21–28
5. Y. Lin, J. Yao, Y. Lei, H. Fu, and L. Wang, Microstructure and Properties of TiB₂-TiB Reinforced Titanium Matrix Composite Coating by Laser Cladding, *Opt. Laser Eng.*, 2016, **86**, p 216–227
 6. M. Keddad and S. Taktak, Characterization and Diffusion Model for the Titanium Boride Layers Formed on the Ti6Al4V Alloy by Plasma Paste Boriding, *Appl. Surf. Sci.*, 2017, **399**(31), p 229–236
 7. L.S. Ma, Y.H. Duan, and P. Li, Microstructure, Growth Kinetics and Some Mechanical Properties of Boride Layers Produced on Pure Titanium by Molten-Salt Boriding, *J. Mater. Eng. Perform.*, 2017, **26**, p 4544
 8. G.K. Sireli, S. Timur, M. Urgen, and A. Erdemir, Electrochemical Boriding of Titanium for Improved Mechanical Properties, *Surf. Coat. Technol.*, 2010, **204**, p 3935–3939
 9. K.G. Anthymidis, G. Stergioudis, and D.N. Tsipas, Boride Coatings on Non-ferrous Materials in a Fluidized Bed Reactor and Their Properties, *Sci. Technol. Adv. Mater.*, 2002, **3**, p 303–311
 10. B. Sarma, N.M. Tikekar, and K.S. Ravi Chandran, Kinetics of Growth of Superhard Boride Layers During Solid State Diffusion of Boron into Titanium, *Ceram. Int.*, 2012, **38**, p 6795–6805
 11. C. Guo, J. Zhou, J. Zhao, B. Guo, Y. Yu, H. Zhou, and J. Chen, Microstructure and Friction and Wear Behavior of Laser Boronizing Composite Coatings on Titanium Substrate, *Appl. Surf. Sci.*, 2011, **257**, p 4398–4405
 12. P. Li, D. Liu, W. Bao, L. Ma, and Y. Duan, Surface Characterization and Diffusion Model Of Pack Borided TB2 Titanium Alloy, *Ceram. Int.*, 2018, **44**, p 18429–18437
 13. M. Keddad, S. Taktak, and S. Tasgetiren, A Diffusion Model for the Titanium Borides on Pure Titanium, *Surf. Eng.*, 2016, **32**, p 802–808
 14. Y. Duan, P. Li, Z. Chen, J. Shi, and L. Ma, Surface Evolution and Growth Kinetics of Ti6Al4V Alloy in Pack Boriding, *J. Alloys Compd.*, 2018, **742**, p 690–701
 15. R. Chaudhari and R. Bauri, A Novel Functionally Gradient Ti/TiB/TiC Hybrid Composite with Wear Resistant Surface Layer, *J. Alloys Compd.*, 2018, **744**(5), p 438–444
 16. B. Sivakumar, R. Singh, and L.C. Pathak, Corrosion Behavior of Titanium Boride Composite Coating Fabricated on Commercially Pure Titanium in Ringer's Solution for Bioimplant Applications, *Mat. Sci. Eng. C*, 2015, **48**, p 243–255
 17. H. Esfahani, F. Dabir, M. Taheri, N. Sohrabi, and M.R. Toroghinejad, Sol-gel Derived Hydroxyapatite Coating on TiB₂/TiB/Ti Substrate, *Surf. Eng.*, 2012, **28**, p 526–531
 18. H. Ding, G. Zhou, T. Liu, M. Xia, and X. Wang, Biotribological Properties of Ti/TiB₂ Multilayers in Simulated Body Solution, *Tribol. Int.*, 2015, **89**, p 62–66
 19. M. Dasa, K. Bhattacharya, S.A. Dittrick, C. Mandal, V.K. Balla, T.S. Sampath Kumar, A. Bandyopadhyay, and I. Manna, In Situ Synthesized TiB-TiN Reinforced Ti6Al4V Alloy Composite Coatings: Microstructure, Tribological and In Vitro Biocompatibility, *J. Mech. Behav. Biomed.*, 2014, **29**, p 259–271
 20. Verein-Deutscher-Ingenieure, *Daimler Benz Adhesion Test VDI 3198*, VDIVerlag, Dusseldorf, 1992, p 7
 21. X.X. Xu, F.L. Nie, J.X. Zhang, W. Zheng, Y.F. Zheng, C. Hu, and G. Yang, Corrosion and Ion Release Behavior of Ultra-Fine Grained Bulk Pure Copper Fabricated by ECAP in Hanks Solution as Potential Biomaterial for Contraception, *Mater. Lett.*, 2010, **64**, p 524–527
 22. B. Sarma and K.S. Ravi Chandran, Accelerated Kinetics of Surface Hardening by Diffusion Near Phase Transition Temperature: Mechanism of Growth of Boride Layers on Titanium, *Acta Mater.*, 2011, **59**, p 4216–4228
 23. N. Makuch, M. Kulka, M. Keddad, S. Taktak, V. Ataibis, and P. Dziarski, Growth Kinetics and Some Mechanical Properties of Two-Phase Boride Layers Produced on Commercially Pure Titanium During Plasma Paste Boriding, *Thin Solid Films*, 2017, **626**, p 25–37
 24. M. Keddad and S. Taktak, Characterization and Diffusion Model for the Titanium Boride Layers Formed on the Ti6Al4V Alloy by Plasma Paste Boriding, *Appl. Surf. Sci.*, 2017, **399**, p 229–236
 25. D. Tijo and M. Masanta, In-Situ TiC-TiB₂ Coating on Ti-6Al-4V Alloy by Tungsten Inert Gas (TIG) Cladding Method: Part-II, Mechanical Performance, *Surf. Coat. Tech.*, 2018, **344**, p 579–589
 26. Y. Lin, Y. Lei, X. Li, X. Zhi, and H. Fu, A Study of TiB₂/TiB Gradient Coating by Laser Cladding on Titanium Alloy, *Opt. Laser Eng.*, 2016, **82**, p 48–55
 27. E. Damerchi, A. Abdollah-zadeh, R. Poursalehi, and M. Salari Mehr, Effects of Functionally Graded TiN Layer and Deposition Temperature on the Structure and Surface Properties of TiCN Coating Deposited on Plasma Nitrided H13 Steel by PACVD Method, *J. Alloys Compd.*, 2019, **772**, p 612–624
 28. C.Y. Lu, W. Diyatmika, BSh Lou, and J.W. Lee, Superimposition of High Power Impulse and Middle Frequency Magnetron Sputtering for Fabrication of CrTiBN Multicomponent Hard Coatings, *Surf. Coat. Technol.*, 2018, **350**, p 962–970
 29. A. Fattah-Alhosseini, A.R. Ansari, Y. Mazaheri, and M.K. Keshavarz, Effect of Immersion Time on the Passive and Electrochemical Response of Annealed and Nano-Grained Commercial Pure Titanium in Ringer's Physiological Solution at 37 °C, *Mat. Sci. Eng. C*, 2017, **71**, p 771–779
 30. A. Fattah-alhosseini, O. Imantalab, and F.R. Attarzadeh, Enhancing the Electrochemical Behavior of Pure Copper by Cyclic Potentiodynamic Passivation: A Comparison Between Coarse- and Nano-Grained Pure Copper, *Metal. Mater. Trans. B*, 2016, **47**, p 2761–2770
 31. A. Shukla and R. Balasubramaniam, Effect of Surface Treatment on Electrochemical Behavior of CP Ti, Ti-6Al-4V and Ti-13Nb-13Zr Alloys in Simulated Human Body Fluid, *Corros. Sci.*, 2006, **48**, p 1696–1720
 32. A. Ebrahimi, H. Esfahani, A. Fattah-alhosseini, and O. Imantalab, In-Vitro Electrochemical Study of TiB/TiB₂ Composite Coating on Titanium in Ringer's Solution, *J. Alloys Compd.*, 2018, **765**, p 826–834
 33. B. Sivakumar, L.C. Pathak, and R. Singh, Response of Boride Coating on the Ti-6Al-4V Alloy to Corrosion and Freting Corrosion Behavior in Ringer's Solution for Bio-implant Application, *Appl. Surf. Sci.*, 2018, **433**, p 1158–1174
 34. R. Singh, M. Martin, and N.B. Dahotre, Influence of Laser Surface Modification on Corrosion Behavior of Stainless Steel 316L and Ti-6Al-4V in Simulated Biofluid, *Surf. Eng.*, 2013, **21**, p 297–306
 35. S. Gnanavel, S. Ponnusamy, L. Mohan, R. Radhika, C. Muthamizhchelvan, and K. Ramasubramanian, Electrochemical Behavior of Biomedical Titanium Alloys Coated with Diamond Carbon in Hanks' Solution, *J. Mater. Eng. Perform.*, 2018, **27**, p 1635
 36. S. Paul and K. Yadav, Corrosion Behavior of Surface-Treated Implant Ti-6Al-4V by Electrochemical Polarization and Impedance Studies, *J. Mater. Eng. Perform.*, 2011, **20**, p 422
 37. H. Ma, S. Chen, B. Yin, S. Zhao, and X. Liu, Impedance Spectroscopic Study of Corrosion Inhibition of Copper by Surfactants in the Acidic Solutions, *Corros. Sci.*, 2003, **45**, p 867–882
 38. H. Luo, C. Dong, X. Li, and K. Xiao, The Electrochemical Behaviour of 2205 Duplex Stainless Steel in Alkaline Solutions with Different pH in the Presence of Chloride, *Electrochim. Acta*, 2012, **64**, p 211–220
 39. H. Luo, S. Gao, C. Dong, and X. Li, Characterization of Electrochemical and Passive Behaviour of Alloy 59 in Acid Solution, *Electrochim. Acta*, 2014, **135**, p 412–419
 40. M. Izadi, T. Shahrabi, and B. Ramezanzadeh, Active Corrosion Protection Performance of an Epoxy Coating Applied on the Mild Steel Modified with an Eco-Friendly Sol-Gel Film Impregnated with Green Corrosion Inhibitor Loaded Nanocontainers, *Appl. Surf. Sci.*, 2018, **440**, p 491–505
 41. H. Akhavan, M. Izadi, I. Mohammadi, T. Shahrabi, and B. Ramezanzadeh, The Synergistic Effect of BTA-Co System on the Corrosion Inhibition of Mild Steel in 3.5 wt% NaCl Solution, *J. Electrochem. Soc.*, 2018, **165**, p C670–C680
 42. F. Rosalbino, R. Carlini, G. Zanocchi, and G. Scavino, Microstructural Characterization and Corrosion Behavior of Lead, Bismuth and Antimony Tellurides Prepared by Melting, *J. Alloys Compd.*, 2013, **567**, p 26–32
 43. A. Fattah-alhosseini, F.R. Attarzadeh, S. Vafaeian, M. Haghshenas, and M.K. Keshavarz, Electrochemical Behavior Assessment of Tantalum in Aqueous KOH Solutions, *Int. J. Refract. Met. Hard Mater.*, 2017, **64**, p 168–175
 44. M. Schönleber, D. Klotz, and E. Ivers-Tiffée, A Method for Improving the Robustness of Linear Kramers-Kronig Validity Tests, *Electrochim. Acta*, 2014, **131**, p 20–27
 45. F.R. Attarzadeh, N. Attarzadeh, S. Vafaeian, and A. Fattah-Alhosseini, Effect of pH on the Electrochemical Behavior of TANTALUM in Borate Buffer Solutions, *J. Mater. Eng. Perform.*, 2016, **25**, p 4199–4209
 46. C. Escrivà-Cerdán, E. Blasco-Tamarit, D. García-García, J. García-Antón, and A. Guenbour, Effect of Potential Formation on the

- Electrochemical Behaviour of a Highly Alloyed Austenitic Stainless Steel in Contaminated Phosphoric Acid at Different Temperatures, *Electrochim. Acta*, 2012, **80**, p 248–256
47. L. Hamadou, L. Ainouche, A. Kadri, S.A.A. Yahia, and N. Benbrahim, Electrochemical Impedance Spectroscopy Study of Thermally Grown Oxides Exhibiting Constant Phase Element Behaviour, *Electrochim. Acta*, 2013, **113**, p 99–108
 48. X. Cheng and S.G. Roscoe, Corrosion Behavior of Titanium in the Presence of Calcium Phosphate and Serum Proteins, *Biomaterials*, 2005, **26**, p 7350–7356
 49. S.O. Gashti, A. Fattah-alhosseini, Y. Mazaheri, and M.K. Keshavarz, Effect of Grain Refinement on Mechanical and Electrochemical Properties of Ultra-Fine Grained AA1050 Fabricated via ARB Process, *J. Manuf. Process.*, 2016, **22**, p 269–277
 50. C. Anandan and L. Mohan, In Vitro Corrosion Behavior and Apatite Growth of Oxygen Plasma Ion Implanted Titanium Alloy β -21S, *J. Mater. Eng. Perform.*, 2013, **22**, p 3507
 51. A. Fattah-alhosseini and S. Vafaiean, Passivation Behavior of a Ferritic Stainless Steel In concentrated Alkaline Solutions, *J. Mater. Res. Tech.*, 2015, **4**, p 423–428
 52. A. Fattah-alhosseini, M. Vakili-Azghandi, M. Sheikhi, and M.K. Keshavarz, Passive and Electrochemical Response of Friction Stir Processed Pure Titanium, *J. Alloys Compd.*, 2017, **704**, p 499–508
 53. M.C. Sellers and E.G. Seebauer, Measurement Method for Carrier Concentration in TiO_2 via the Mott–Schottky Approach, *Thin Solid Films*, 2011, **519**, p 2103–2110
 54. B. Roh and D. Macdonald, Effect of Oxygen Vacancies in Anodic Titanium Oxide Films on the Kinetics of the Oxygen Electrode Reaction, *Russ. J. Electrochem.*, 2007, **43**, p 125–135
 55. A. Fattah-Alhosseini, O. Imantalab, and G. Ansari, The Role of Grain Refinement and Film Formation Potential on the Electrochemical Behavior of Commercial Pure Titanium in Hanks' Physiological Solution, *Mat. Sci. Eng. C*, 2017, **71**, p 827–834
 56. L. Hamadou, A. Kadri, and N. Benbrahim, Characterisation of Passive Films Formed on Low Carbon Steel in Borate Buffer Solution (pH 9.2) by Electrochemical Impedance Spectroscopy, *Appl. Surf. Sci.*, 2005, **252**, p 1510–1519
 57. B.S. Covino, Jr., S.D. Cramer, J.P. Carter, and D. Schlain, Corrosion of Titanium Diboride, *J. Less Common Met.*, 1975, **41**, p 211–224
 58. M. Pourbaix, *Atlas of Electrochemical Equilibriums in Aqueous Solutions*, Pergamon Press, Oxford, 1966, p 213–222

Publisher's Note Springer Nature remains neutral with regard to jurisdictional claims in published maps and institutional affiliations.